Elias N. Mansbach[1], Jay Shah[1], Wyn Williams[2], Clara Maurel[3,1], James F. J. Bryson[4], Benjamin P. Weiss[1]

[1]Department of Earth, Atmospheric, and Planetary Science, Massachusetts Institute of Technology, Cambridge, MA, USA

[2]School of GeoSciences, University of Edinburgh, Edinburgh, UK

[3]CNRS, Aix Marseille Université, IRD, INRAE, CEREGE, Aix-en-Provence, France

[4]Department of Earth Sciences, University of Oxford, Oxford, UK

Corresponding author: Elias Mansbach (mansbach@mit.edu)

Key Points:

- The meteoritic iron-nickel mineral tetrataenite can carry robust records of ancient planetary magnetism
- Due to its high uniaxial anisotropy, tetrataenite forms single domain or multidomain states without a transitional single-vortex state
- Tetrataenite occupies the single domain state with coercivities of 10^2-10^3 mT for grain lengths between ~10 and 160 nm

Abstract

Paleomagnetic studies of meteorites constrain the evolution of magnetic fields in the early solar system. These studies rely on the identification of magnetic minerals that can retain stable magnetizations over 4.5 billion years (Ga). The ferromagnetic mineral tetrataenite ("-$Fe_{0.5}Ni_{0.5}$) is found in iron, stony-iron and chondrite meteorite groups. Nanoscale intergrowths of magnetostatically-interacting tetrataenite have been shown to carry records of paleomagnetic fields. Tetrataenite can also occur as isolated, non-interacting grains in many meteorite groups. Here we study non-interacting tetrataenite to establish the grain size range over which it can retain magnetization that is stable over solar system history. We present the results of analytical calculations and micromagnetic modelling of isolated tetrataenite grains with various sizes and geometries. We find that tetrataenite forms a stable single domain state for grain lengths between ~10 and 160 nm dependent on its axial ratio. It also possesses a magnetization resistant to viscous remagnetization over the lifetime of the solar system at 293 K. At smaller grain sizes, tetrataenite is superparamagnetic while at larger grain sizes, tetrataenite's lowest energy state is a lamellar two-domain state that is stable over Ga-scale timescales. Unlike many other ferromagnetic minerals, tetrataenite does not form a single-vortex domain state due to its large uniaxial anisotropy. Our results show that both single domain and two-domain tetrataenite carry extremely stable magnetization and therefore are promising for paleomagnetic studies.

Plain Language Summary

Meteorites are fragments of small bodies created during the early solar system and contain records of how planets formed and small bodies evolved. A way to further this understanding is by studying the magnetic fields recorded by these rocks. To do so requires the identification of magnetic minerals capable of retaining a record of an ancient field (in the form of a measurable magnetization) over the past 4.5 billion years. One mineral that is a potentially reliable recorder is tetrataenite (ordered Fe-Ni metal). The stability of the grain's magnetization is tied to its shape and size. Here, we present the results of analytical calculations and numerical modeling of tetrataenite grains with various shapes and sizes to determine the conditions under which tetrataenite magnetization is stable over the lifetime of the solar system. We find that tetrataenite occupies a single-domain state (in which all magnetization is uniform throughout the grain volume) at grain lengths between ~10-160 nm depending on the elongation of the grain. Above those sizes, tetrataenite forms a stable two-domain structure. We find that single domain and two domain tetrataenite are both viable carriers of magnetization that can be stable over the lifetime of the solar system.

1 Introduction

Paleomagnetic studies of extraterrestrial materials have sought to measure the ancient intensity of magnetic fields in the early solar system to elucidate solar nebular and planetary evolution processes (Weiss et al., 2010). Analyses of chondrites have demonstrated that magnetic fields were present in the protoplanetary disk and might have played an important role in mass and angular momentum transport (Borlina et al., 2021; James F. J. Bryson et al., 2020; Cournede et al., 2015; Fu et al., 2014b; Weiss et al., 2021). Paleomagnetic investigations of basaltic achondrites and iron meteorites, which formed as the result of widespread melting and differentiation on their parent bodies, provide evidence that the metallic cores of early small bodies generated dynamo magnetic fields (J. F. J. Bryson et al., 2014a; J. F. J. Bryson et al., 2019; J. F. J. Bryson et al., 2017; Fu et al., 2012; Maurel et al., 2020; Maurel et al., 2021; Nichols et al., 2020; Nichols et al., 2016; Weiss et al., 2008a).

The ability to conduct reliable magnetic studies of early solar system materials is contingent on the presence of magnetic carriers capable of retaining a natural remanent magnetization over >4.5 billion years (Ga). Such carriers are usually thought to be in the single domain [SD; (Néel, 1955)] or single vortex (SV) states (Einsle et al., 2016; Shah et al., 2018). The SD and SV states are typically the most resistant to remagnetization because of their higher coercivities and their long magnetic relaxation times that exceed the age of the solar system. In meteorites and lunar samples, the ferromagnetic minerals kamacite (-$Fe_{1-x}Ni_x$ for x 0.05) (Garrick-Bethell & Weiss, 2010; Gattacceca et al., 2014; Weiss et al., 2010), pyrrhotite ($Fe_{1-x}S$ for $x < 0.17$) (Weiss et al., 2008b), and magnetite (Fe_3O_4) (Fu et al., 2014a; Gattacceca et al., 2016) have been found to hold paleomagnetic records. Previous analytical calculations based on Neel theory and micromagnetic modeling (e.g., section 2) have shown that kamacite and magnetite grains are in the SD state from ~15 to ~300 nm (Muxworthy &

Williams, 2015; Shah et al., 2018), and ~30 nm to ~1000 nm (Butler & Banerjee, 1975b; Muxworthy et al., 2003; Muxworthy & Williams, 2006; Nagy et al., 2017), respectively depending on the axial ratio of the grain, which is the ratio of the grain width to grain length. Above that size range, magnetite and kamacite occupy an SV or multidomain (MD) state. The superparamagnetic (SP) to SD transition of pyrrhotite has been calculated to be 46 nm (Dunlop, 2021), but the SD to MD transition is not well characterized. Bitter pattern observations of domain states place the SD to MD transition at 1.6 µm (Soffel, 1976) and hysteresis properties suggest the mineral is SD for grains < 3 µm (Clark, 1984). Pyrrhotite in the SV state has not been reported in natural samples, but the formation of vortices has been invoked as a potential explanation for the decrease in saturation remanence exhibited by pyrrhotite upon heating (Dunlop, 2021). Analytical calculations have also been performed for greigite (Fe_3S_4), which occupies the SD state for grains 10 nm to 250 nm (Ricci & Kirschvink, 1992).

Tetrataenite (''-$Fe_{0.5}Ni_{0.5}$) is a tetragonal mineral [whose crystallographic long to short axis ratio, $c/a = 1.0036$, (Albertsen, 1981)] found naturally in meteorites that forms crystals with microcoercivities reaching > 1 T (Uehara et al., 2011). The paleomagnetic record carried by tetrataenite has been investigated in IIE (Maurel et al., 2020; Maurel et al., 2021), IVA (J. F. J. Bryson et al., 2017) and IAB iron meteorites (J. F. J. Bryson et al., 2014b; Nichols et al., 2018), main group pallasites (J. F. J. Bryson et al., 2015; Nichols et al., 2016), mesosiderites (Nichols et al., 2020), and an H chondrite (J. F. J. Bryson et al., 2019). The tetrataenite grains analyzed in these meteorite groups are located in the "cloudy zone" microstructure, a nanoscale intergrowth of <500 nm diameter tetrataenite "islands" in an antitaenite matrix (Nichols et al., 2020) located near the rims of zoned Fe-Ni grains (Fig. 1a). The cloudy zone forms as a result of spinodal decomposition of taenite (-$Fe_{1-x}Ni_x$) during slow cooling (<10,000 ^{o}C Ma^{-1}) below 400 ^{o}C (Maurel et al., 2019). If the slow cooling rate is maintained, the portion of the adjacent taenite rim with >40% Ni and cloudy zone islands (initially made of Fe-Ni taenite) order to tetrataenite at 320 ^{o}C. The size of the tetrataenite grains is dependent on cooling rate, with smaller grains forming during more rapid cooling.

Little is known about the domain states and grain size range for which tetrataenite magnetization is stable against external fields or viscous remagnetization at ambient temperatures. Einsle et al. (2018) studied the magnetic remanence acquisition of CZ islands by simulating the ordering process of tetrataenite using micromagnetic modeling. The authors found that SV taenite islands with lengths of 82-92 nm would transition to SD tetrataenite via an intermediate two-domain state. The two-domain state becomes a SD state due to the annihilation of the domain wall through the presence of an external field and/or island-island magnetostatic interactions. Once such tetrataenite grains are placed in the SD state, a field >1 T is needed to re-nucleate the domain wall.

Einsle et al. (2018) focused primarily on remanence acquisition mechanisms of the cloudy zone and the effect of magnetostatic interactions between tetrataenite

grains. However, the magnetic behavior of isolated, non-interacting tetrataenite has yet to be addressed and would provide an apt comparison to the behavior of interacting tetrataenite grains to elucidate the effect of magnetostatic interactions on tetrataenite magnetization. Non-interacting tetrataenite is found in the form of inclusions in silicates in primitive achondrites [Fig. 2c; (Mansbach et al., 2022)] and in the meteoritic microstructure plessite in ordinary chondrites (Goldstein & Michael, 2006; Reisener & Goldstein, 2003; Willis & Goldstein, 1983) and other iron meteorite groups [Fig. 2b; (Buchwald, 1975)]. Plessite is a micromagnetic intergrowth of kamacite and taenite or tetrataenite, with microcoercivities > 100 mT (Goldstein & Michael, 2006; Uehara et al., 2011). While the tetrataenite grains in primitive achondritic silicates and chondritic/iron meteorite plessite are not neighboring and are unlikely to experience magnetostatic interactions from other tetrataenite grains, the grains border or are embedded in kamacite (Willis & Goldstein, 1983). The effect of interactions between kamacite and the tetrataenite in these microstructures are unknown, and therefore we use the term non-interacting tetrataenite to indicate tetrataenite magnetization not affected by other tetrataenite grains only.

Here we analyze the magnetic stability and magnetic properties of individual tetrataenite grains via analytical calculations and micromagnetic modeling. We focus on tetrataenite grains with various lengths and axial ratios (A), to determine under what conditions tetrataenite is stable in terms of resistance to remagnetization by external fields (coercivity) and relaxation time. Both high coercivities and long relaxation times are needed to ensure that the natural remanent magnetization is not reset over $>$4.5 Ga. These results will aid in identifying tetrataenite in meteorites, such as plessite-bearing meteorites, that can be reliably studied and provide a comparison with the observations from cloudy zone studies.

2 Analytical Calculation and Micromagnetic Simulation Methodology

We now describe the methodology for our analytical calculations and micromagnetic modeling of the domain states in tetrataenite. We start by discussing the analytical formulas based on Néel theory that predict the SP (relaxation time $>$ 4.5 Ga) to SD transition and SD to MD transition. Analytical relationships provide an intuitive understanding of the principles of energy conservation. However, Néel theory is unable to predict the existence of an SV state or other metastable states. Therefore, we also conduct micromagnetic calculations to assess the possible existence of an SV state and the critical size range over which it might form. Together, micromagnetic modeling and analytical calculations provide a holistic view of the sizes and shapes of individual tetrataenite grains that are magnetically stable and therefore useful for paleomagnetism.

2.1 Analytical Calculations

To determine the SP to SD threshold size for tetrataenite at various axial ratios, we consider a modification of the Néel-Arrhenius equation which defines the relaxation time as the ratio of magnetic anisotropy energy, U_M to thermal energy,

U_T:

$$\tau = \frac{U_M}{U_T} = \frac{1}{C} e^{\frac{E}{k_B T}} = \frac{1}{C} e^{\frac{v H_c \mu_0 M_s}{2 k_B T}}$$

where τ is the relaxation time, C is a frequency factor ~10^9 Hz, $v = l^3 A^2$ is the grain volume where l is the length of the long axis, H_c is the microscopic coercivity, μ_0 is the permeability of free space, M_s is the saturation magnetization [1.39 $\times 10^6$ A m^{-1} for tetrataenite; (Néel et al., 1964)], k_B is Boltzmann's constant, and T is temperature in K [see Equation 6 in (Evans & Mcelhinny, 1969)] .

In tetrataenite, magnetocrystalline anisotropy dominates over shape anisotropy. This is because the microcoercivity due to magnetocrystalline anisotropy [$H_M = 2K/\mu_0 M_s$ where $K = 1.37 \times 10^6$ J m^{-3} (Einsle et al., 2018) is the magnetocrystalline anisotropy constant] is larger than the microcoercivity due to shape anisotropy [$H_S = M_s\, N$ where N is the difference in demagnetization factors along the short and long grain axes]. In our calculations we choose to consider the effects from both magnetocrystalline anisotropy and shape anisotropy, because $H_M = 1.57 \times 10^6$ A m^{-1} and $H_S = 1.39 \times 10^6\ N$ A m^{-1} where $0 \leq N \leq 0.5$ remain within an order of magnitude. We define the total microscopic coercivity $H_T = H_M + H_S$ and substitute this for H_c in Eq. (1). We assume in the definition of H_T that the shape and magnetocrystalline easy axes are aligned. This is almost certainly not the case for all grains, but a sum of the two anisotropies places a lower bound on the SP-SD transition.

Rearranging Eq. (1), we find:

$$l_S = \left[\frac{2 k_B T \ln \ln (\ \mathrm{C})}{A^2 \left(2K + \mu_0 M_S^2\, N\right)} \right]^{\frac{1}{3}}$$

We define the critical relaxation time for the SP-SD transition to be $\tau = 4.5$ Ga, since we are concerned with magnetic records from meteorites that are stable over the lifetime of the solar system. Conventionally, the SP-SD transition is often defined as stable magnetization on the laboratory time scale [100 s; (Tauxe, 2010)], although since the grain length is dependent on ln $(\tau)^{1/3}$, the SP-SD transition at 4.5 Ga and 100 s differ by only a factor of ~2.

We define the SD-MD threshold to be the grain length at which the energies of an SD state and a two-domain state are equal (Dunlop & Özdemir, 1997). Above the critical SD size, it is energetically favorable for the grain to nucleate a domain wall rather than retaining a state of uniform magnetization with high magnetostatic energy (Dunlop & Özdemir, 1997). Following Equation 5.28 in Dunlop and Özdemir (1997) and substituting for the domain wall energy $[2\pi(K A_{\mathrm{ex}})^{1/2}$, where $A_{ex} = 1.13 \times 10^{-11}$ J m^{-1} (Einsle et al., 2018) is the ex-

change energy], we find that the critical length of the long axis of a cuboid can be expressed as :

$$l_M = \frac{8\pi\sqrt{KA_{\rm ex}}}{\mu_0 N M_s^2}$$

where N is the demagnetization factor along the elongated axis. The demagnetization factor is dependent on the axial ratio, ranging from 1/3 when the grain is equant to zero when the grain is an infinitely elongated rectangular prism (Aharoni, 1998). The demagnetization factor is considered only along the elongated axis as it is the minimum energy direction of magnetization. Demagnetization factors for Eqs. (2) and (3) are calculated using Equation 5 from Aharoni (1998) for a cuboid with the two minor axes being the same length (see Supplementary Text).

Assuming the lamellar shape of the domains persists to larger grains sizes, the analytical solution for the transition from a two-domain grain to a three-domain grain and to higher domain states can be obtained from the extension of Equation 5.27 in Dunlop and Özdemir (1997) which defines the transition from an SD state to a two-domain state. By analogy, the transition from two domains to three domains occurs when the energy of the two- and three-domain states are the same, and more generally when the energy of an n-domain grain is the same as an n+1- domain grain. Using the approximation that the demagnetizing energy of an n domain grain is $1/n$ times the demagnetization energy of an SD grain [Equation 5.3 in Dunlop and Özdemir (1997)], the transition from an n domain grain to an n+1 domain grain occurs when

$$\underbrace{\tfrac{1}{2}\mu_0 v \mathrm{NM}_s^2 \tfrac{1}{n}}_{n-\textit{domain demagnetization energy}} + \underbrace{2\pi\sqrt{KA_{\rm ex}}\mathrm{wu}(n-1)}_{\textit{Energy to form } n-1 \textit{ domain walls}}$$

$$= \frac{1}{2}\mu_0 v \mathrm{NM}_s^2 \frac{1}{n+1} + 2\pi\sqrt{KA_{\rm ex}}\mathrm{wun}$$

where w and u are the width and height of the grain respectively and equal lA if the grain is a rectangular prism. Substituting $v = l^3A^2$ and solving for l, we find:

$$l_n = \frac{4\pi\sqrt{KA_{\rm ex}}}{\mu_0 \mathrm{NM}_s^2\left(\frac{1}{n} - \frac{1}{n+1}\right)}$$

(5)

and, therefore, the two-domain to three-domain transition ($n = 2$) occurs at

$$l_2 = \frac{24\pi\sqrt{KA_{\rm ex}}}{\mu_0 \mathrm{NM}_s^2}$$

. (6)

The single vortex state is not predicted by Néel theory. While attempts have been made to analytically calculate the transition from SD to a circular spin state [e.g. (Butler & Banerjee, 1975a)], the circular spin state modeled has no vortex core that can account for the remanence of the grain. However, the SV threshold can be determined using micromagnetic modeling.

2.2 Micromagnetic Modeling

We conducted micromagnetic modeling of individual tetrataenite grains using the Micromagnetic Earth Related Robust Interpreted Language Laboratory [MERRILL version 1.6.4) software (Conbhuí et al., 2018)]. MERRILL is an open-source software package that uses finite-element modeling to simulate the three-dimensional magnetic structure of a tetrahedrally-meshed grain. MERRILL finds the magnetization state by solving for the orientations of an array of dipoles that have the minimum magnetic energy associated with exchange, anisotropy, Zeeman, and internal demagnetization fields. A full description of MERRILL can be found in Conbhuí et al. (2018).

Cuboid grain meshes were created using the meshing software MeshRRILL (Conbhuí et al., 2018) with a tetrahedral element size of 3 nm, which is the magnetic exchange length of tetrataenite as defined by Equation 12 in Conbhuí et al. (2018). The element size was limited to the exchange length to ensure that spatial variations of the magnetization within a grain were correctly accounted for in the calculation of the total free magnetic energy. Magnetic parameters for tetrataenite were taken from Néel et al. (1964) and Einsle et al. (2018), with K, A_{ex}, and M_s defined in Section 2.1. All simulations were calculated at room temperature $T = 293$ K. While meteorites likely experiences temperatures ~150-280 K while in the asteroid belt and transfer to Earth (Weiss et al., 2010), grains stable at 293 K will be almost always be stable at the lower temperatures since there is less thermal energy (barring phase transformations). We are not aware of any reports of tetrataenite crystallographic phase transitions at such low temperatures.

To determine the SP-SD threshold size, each element of the mesh was initialized with a randomly oriented magnetic moment of equal magnitude. Simulations were conducted with the magnetic easy axis oriented parallel to the elongated [001] axis to be consistent with our analytical calculations. Once initialized, MERRILL minimized the total energy of the system using a modified conjugate gradient method (Fabian & Shcherbakov, 2018). For each grain size and axial ratio modeled, 100 least-energy magnetization (LEM) solutions were completed, each with a different randomized initial state, to calculate the least-energy state (i.e., to identify the global minimum energy state). To calculate the energy barrier for viscous remagnetization, we considered two different end-member magnetization states with the lowest energy but opposite moment directions. These two configurations were passed into MERRILL, which used a nudged elastic band (NEB) method to determine the minimum-action path between the end-

member states (Fabian & Shcherbakov, 2018). Our calculations considered 100 magnetization steps between the two states. The energy barrier to remagnetization was calculated as the energy difference between the saddle point on the minimum-energy path and the initial state, E. The relaxation time was then determined using the Néel-Arrhenius equation (Eq. 1) with $T = 293$ K. The critical relaxation time was set at 4.5 Ga to ensure that any magnetization would be retained over the lifetime of the solar system.

We determined the threshold size for a single-to-nonuniform domain (e.g., SV or MD) state by identifying the grain size at which the least-energy state from 100 random initial guesses transformed from a SD state to a nonuniform state. The resistance of these nonuniform states to viscous remagnetization was determined by calculating NEB paths and relaxation times in a similar manner to the SP-SD threshold.

Simulated hysteresis loops for grains at various axial ratios with sizes above the SP-SD threshold, including nonuniform states, were created using MERRILL to determine the behavior of the states in response to an external field. The least energy state identified for each grain geometry was used as the initial configuration. The energy of the system was then minimized in the presence of subsequent increasing external fields along the easy axis direction. The resulting least-energy state after each minimization was the initial configuration for the following external field step. External fields were increased in steps of 10 mT from 0 mT to the saturating field (depending on the geometry of the grain). The external field was then decreased in steps of 10 mT to the saturating field value in the opposite direction and increased again to reach the positive saturating field.

All simulations were conducted on the MIT Engaging Cluster using Centos 7 cores with 128 GHz random access memory (RAM). The SP-SD threshold size was determined for axial ratios between 0.1 and 1 in steps of 0.1. The memory demands of MERRILL on our computation facilities limited our calculations of the threshold size for the SD-to-nonuniform domain state to axial ratios between 0.55 and 1 in steps of 0.05. The largest grain modeled was a 120 nm cube with a volume 1,728,000 nm^3 comprising 269,855 elements.

3 Results

3.1 Analytical and Micromagnetic Modeling of Tetrataenite Domain States

The domain state behavior of tetrataenite as a function of axial ratio and length is shown in Figure 2. Both the analytical calculations for the SP-SD transition and micromagnetic modeling show a monotonic increase of the threshold size with decreasing axial ratio. This trend follows a dependence of $A^{-2/3}$ as shown in Eq. (2). Because of the dominant magnetocrystalline anisotropy, the threshold volume of the grain is nearly constant with axial ratio—in contrast to the SP-SD threshold for kamacite and magnetite. Magnetite's high saturation magnetization compared to its magnetocrystalline anisotropy constant [4.80×10^5 A m^{-1} and -1.35×10^4 J m^{-3} respectively; (Dunlop & Özdemir, 1997)] leads to this

mineral being dominated by shape anisotropy at nearly all axial ratios. Thus, the SP-SD threshold size subsequently decreases with increasing elongation to A = ~0.6 before growing again with further elongation (Butler & Banerjee, 1975b). A similar trend in the SP-SD threshold was found for kamacite (Butler & Banerjee, 1975a), which has a high saturation magnetization compared to its magnetocrystalline anisotropy constant [1.715 $\times$ 10^6 A m^{-1} and 4.8 $\times$ 10^4 J m^{-3}, respectively (Dunlop & Özdemir, 1997)]. The transition from SP to SD for tetrataenite results in a sharp increase in relaxation time. For a cube (SP-SD threshold of 6 nm), the relaxation time jumps from ~2,560 years at 5 nm to 3.34 $\times$ 10^8 Ga at 6 nm due to the increase in the energy barrier when the SD state is reached (Supplement Movie 1).

Our micromagnetic simulations show that unlike magnetite and kamacite, which transition through a SV state prior to a MD state as their grain size increases (Muxworthy & Williams, 2006, 2015; Shah et al., 2018), tetrataenite does not form a single vortex state but instead transitions directly from a "flowering" single domain state to a two-domain state (Fig. 3). This is due to the substantially higher magnetocrystalline anisotropy constant of tetrataenite compared to kamacite and magnetite (28 and 100 times larger, respectively). The large magnetocrystalline anisotropy prohibits the individual dipole moments associated with each element node from being canted relative to the magnetic easy axis. This prevents the formation of a vortex core, forcing the least energy state instead to be two domains separated by a nucleated grain wall. The absence of a single vortex state in tetrataenite is in agreement with the results from Einsle et al. (2018), who found that tetrataenite grains formed a two-domain state prior to the destruction of the domain wall due to island-island interactions and/or external fields. In this sense, tetrataenite conforms much better to the predictions of classical Neel theory compared to magnetite and kamacite. It should be noted that the "flower" state is not truly SD as the magnetization is not uniform across the whole grain, but we treat it as akin to the SD state instead of a pseudo single domain state since the vast majority of the magnetization is uniform (>99% of the saturation magnetization of the grain). Denoting the "flower" state as SD is consistent with other micromagnetic modeling studied [e.g. (Muxworthy & Williams, 2015)].

Unlike for the SP-SD threshold, we find a modest mismatch between analytical and micromagnetic modeling solutions for the SD to MD threshold (Fig. 2). The analytical solution consistently overestimates the transition size compared to the modeling results. This is consistent with the difference between micromagnetic modeling and analytical results reported for magnetite, since the approach of (Butler & Banerjee, 1975c) assumes a uniform SD state transitioning to a two-domain state, which does not accurately represent the "flower" state seen at larger SD grain sizes or the nonuniform state [Fig. 3, (Muxworthy & Williams, 2006)].

We tested the consistency of our micromagnetic results by running simulations for tetrataenite spheres. The SD-to-two-domain threshold for a sphere is 80 nm

diameter, higher than the critical length for a cube (Fig. 2b). However, the domain transition occurs at a comparable volume (sphere transition at 102% volume of the cube), highlighting that the transition occurs at a critical volume such that the equivalent length is shape-dependent. We present our results for cuboids to be consistent with previous micromagnetic modeling work [e.g. (Butler & Banerjee, 1975c; Muxworthy & Williams, 2015)].

3.2 Magnetic Stability of Tetrataenite Domain States

The magnetic stability of a grain is a measure of its resistance to changes in its magnetization state, such as direction or structure, which might be initiated by changing external fields or from viscous relaxation. We address the question of tetrataenite magnetic resistance to field and viscous decay separately in the following subsections.

3.2.1 Magnetic Relaxation Times of Tetrataenite

To determine the magnetic relaxation time of SD and two-domain tetrataenite, we calculated NEB paths using MERRILL to quantify the energy barrier between two states. For all tetrataenite grains that fall into the SD stability field (Fig. 2), the energy barrier between anti-aligned magnetizations along the magnetic easy axis is associated with a relaxation time > 4.5 Ga. For a 30 nm and 50 nm cube, the NEB path (Fig. 4a, b) quantifies the energy barrier to be 3,095 $k_B T$ and 8,280 $k_B T$ respectively, corresponding to enormous relaxation times of $\sim 1 \times 10^{1344}$ yr and $\sim 9 \times 10^{3595}$ yr. The magnetization of the grains are flipped via the nucleation of a domain wall in one corner of the grain, which subsequently propagates through the grain, creating a metastable two-domain state in each NEB path (Fig. 4a, b; Supplementary Movie 2 and 3). Due to the presence of a metastable state, another NEB path was calculated between the initial single domain state and the metastable state to increase the resolution of the energy barrier. Because the energy barrier between the metastable two-domain state and the SD state is $\sim$1000 $k_B T$ ($\sim 6 \times 10^{417}$ yr), a grain geometry that normally falls in the SD stability field (Fig. 2) but is placed in a two-domain state will be highly resistant to thermal fluctuations relaxing it to the SD state.

For an 80-nm cube that falls into the two-domain stability field (Fig. 2), we modeled the energy barriers between combinations of two-domain and SD states. The energy barrier between an initial two-domain state and a higher-energy SD state is $\sim$25,000 $k_B T$, though the path involves multiple metastable states (Fig. 4f, Supplement Movie 4). Recalculating the energy barrier between the two-domain state and the first metastable state, which is a two-domain state with a curved domain wall, results in a $\sim$9,000 $k_B T$ barrier. Modelling the energy barrier between two perpendicularly aligned two-domain states also shows the presence of metastable states with energy barriers consistent with relaxation times > 4.5 Ga (Fig. 4e, Supplement Movie 5). Thus, two-domain tetrataenite is extremely stable against viscous relaxation.

An 80 nm cube placed in an SD state, which has a higher energy than the two-

domain state, can transition through multiple metastable states to either an anti-aligned SD state or a two-domain state separately (Fig. 4c, d; Supplement Movies 6-7). The first metastable state for both NEB paths is a two-domain state with a curved domain wall that segments the grain into two domains that occupy ~12.5% and ~87.5% of the grain volume each (Fig. 4c, d inset). The energy barrier between the initial SD state and the metastable state is $> 4{,}000$ $k_B T$. Therefore, a grain with a size and shape that would fall into the two-domain stability field but is placed in an SD state is resistant to viscous decay over time periods relevant for paleomagnetic studies.

3.2.2 Simulated hysteresis loops

Due to the general lack of a pseudo single domain state, we find that the hysteresis behavior of single domain tetrataenite follows Néel theory (Néel, 1955). The grain occupies a uniform state until a critical field is applied antiparallel to the magnetization, resulting in a reversal of the magnetization direction (Figure 5a, Supplement Movie 8). Barring any heating, it is therefore unlikely that a tetrataenite grain in the SD stability field would be found in a two-domain state despite that state being resistant to thermal relaxation to the SD state (Section 3.2.1). The microcoercivity of tetrataenite increases with decreasing grain size for a constant axial ratio (Fig. 6), suggesting that higher fields are necessary to remagnetize smaller tetrataenite grains. This is possibly due to an increased degree of "flowering" in the SD state at larger grain sizes. The microcoercivity of tetrataenite is also influenced by the axial ratio, with elongated grains requiring higher fields to flip their magnetization direction. This is expected as elongation in the direction of the magnetic easy axis inhibits the ability of the individual element magnetization to coherently rotate in the direction of an external field due to shape anisotropy.

Traditionally, MD grains are considered poor paleomagnetic recorders in part due to the ease of domain states changing in response to external fields by domain wall motion (Nagy et al., 2019). However, two-domain tetrataenite easily resists domain wall displacement at external field strengths relevant for planetary or planetesimal dynamos [< 300 µT; (Maurel et al., 2021)]. Application of even a 1 mT external field creates a change in magnetization of $< 2\%$ from domain wall movement (Fig. 5b). However, the presence of stronger external fields causes the domain with magnetization parallel to the field to grow, displacing the domain wall in a direction perpendicular to the applied field. The field-aligned domain continues to grow at the expense of the antiparallel domain as the field increases until a critical field, H_W, is reached at which the domain wall is destroyed and the grain becomes uniformly magnetized (see Supplementary Movies 9 and 10). This behavior was also observed by Einsle et al. (2018) for tetrataenite in the cloudy zone, who found that the domain wall could be destroyed by island-island interactions or an external field, although our results show that the required intensity of the external field means it could not be from a planetary or planetesimal dynamo. The critical field H_W is dependent on the axial ratio and grain size, with increasing grain size and larger axial ratios

possessing higher H_W values.

For a two-domain tetrataenite grain that transitions to an SD state due to an external field, the reduction of the external field to zero does not place the grain back in a two-domain state. Instead, once the field is eliminated, the initially two-domain grain will continue to occupy a uniform state. This suggests that the uniform state is highly stable even though it is not the least-energy state for the grain geometry. This pattern was observed for all two-domain grains modeled and is a potentially important aspect of cloudy zone tetrataenite magnetization evolution (Section 4.2). Conversely, a SD state cannot be placed in a two-domain state through the application of an external field.

3.3 Observations of Two-Domain Tetrataenite

Tetrataenite grains are found in meteoritic plessite, which forms from the decomposition of martensite into an intergrowth of kamacite and taenite/tetrataenite [Supplementary Text, (Goldstein & Michael, 2006)]. The coarseness of plessite structures is primarily dependent on the bulk Ni content of the meteorite and its cooling rate (Buchwald, 1975; Goldstein & Michael, 2006). Duplex plessite is a coarse-grained plessite, where taenite/tetrataenite grains are separated by several µm of kamacite unlike in the nm-scale cloudy zone. No magnetostatic interactions are expected between tetrataenite grains, but we cannot rule out the existence of exchange interactions between tetrataenite grains and surrounding kamacite based on current knowledge. The tetrataenite grains can be hundreds of nm to a few µm in size.

We collected X-ray photoemission electron microscopy (XPEEM) images of duplex plessite in the ungrouped Bacubirito iron meteorite using Beamline 11.0.1 at the Advanced Light Source, Lawrence Berkeley National Laboratory (Supplementary Text). Our X-ray circular magnetic dichroic (XMCD) images produced from the XPEEM data (Stöhr et al., 1998) show the magnetization of kamacite and individual taenite/tetrataenite grains along the X-ray beam direction (Fig. 7). We applied a magnetic field of increasing intensity in steps of ~50 mT up to 324 mT and collected XMCD images at each step. We find that the uniformly-magnetized individual taenite/tetrataenite grains have coercivities between 250 and 324 mT (Supplementary Fig. S4, 5). Moreover, the grains have an average 48 wt% Ni content (measured using electron dispersive spectroscopy). While Ni composition alone cannot distinguish between taenite and tetrataenite, reported coercivities for taenite formed from the annealing of ~30 nm tetrataenite in the Santa Catharina ataxite are less than 10 mT (Dos Santos et al., 2015). Therefore, we interpret the measured coercivities of the Ni-rich grains to be indicative of tetrataenite and not taenite.

XMCD images show that all of the kamacite is MD (Fig. 7). The tetrataenite grains are either SD or MD, although some grains have XMCD signals that cannot be distinguished from the kamacite. Four tetrataenite grains show uniform magnetization and have lengths and axial ratios that place them in the two-domain stability field in Figure 2A close to the SD-two domain transition ac-

cording to analytical calculations. There are multiple reasons why these grains appear SD but fall into the calculated two-domain stability field: (1) The analytical calculations do not accurately reflect the SD-two domain transition, which is suggested by the mismatch between the MERRILL results and the analytical calculations. Grains of this size and geometry were unable to be modeled using MERRILL due to computational limits; (2) The grains were initially two-domain but later placed into an SD state due to an external field; or (3) The calculated grain lengths and axial ratios are not representative of the true morphology of the grains since we are viewing a two-dimensional slice of the plessitic microstructure. This final caveat is important for all tetrataenite grains discussed.

A two-domain grain with a length of 400 nm and axial ratio of 0.57 was observed (Fig. 7 magenta box), showing that the two-domain state is achievable in nature under non-interacting conditions and relevant grain geometries. The size and axial ratio of the grain places it in the two-domain stability field (Fig. 2). Moreover, finding a two-domain state implies that the meteorite was not substantially remagnetized at fields above the coercivity of the grain (Section 3.2.2). This rules out the possibility that the aforementioned single domain grains were initially in a two-domain grain and had their domain wall destroyed by an external field.

Other tetrataenite with clear XMCD signals are in other MD states, consisting of more than two domains or having more complex domain structures than the described two-domain grain in the previous paragraph (Fig. 7). One grain, highlighted by the orange box in Figure 7, has a size and shape comparable to that of neighboring uniformly-magnetized grains, while two other MD grains are very elongated ($A < 0.25$) and are larger than the other grains imaged (Fig. 2). The observation of an MD grain of a size similar to the size of uniformly magnetized grains is inconsistent with our understanding of individual tetrataenite domain states as a function of grain geometry. We see three possible explanations: (1) Exchange interactions with the kamacite matrix that are currently incompletely understood; (2) Our micromagnetic modelling does not account completely for the geometry of the grain. Note that the domain threshold sizes are dependent on the morphology of the grain (Section 3.1); (3) The grains are larger than they appear on the cut surface of the sample. It should be noted that XPEEM only provides the magnetization from the top 5 nm (J. F. J. Bryson et al., 2014b) of the sample.

XMCD images of the tetrataenite grains after the application of a 324 mT field show that the magnetization of the grains are aligned in a similar direction relative to the X-ray beam (Fig. 7c). The uniformly-magnetized grains still retain a uniform magnetization and the grains with more than two domains, while still showing multiple domains, appear to be mostly magnetized in the same direction as the SD grains. However, the previously identified two-domain grain now shows a complex domain structure consisting of three to four domains with curved domain walls. This is unexpected based on our simulated hysteresis

loops, which suggested that the grain should remain in a two-domain state until the domain wall is destroyed, creating an SD structure. We do see metastable states with curved domains in our NEB paths in Figure 4, and therefore propose that the grain is in a metastable state or that our micromagnetic modelling cannot account for all interactions between the external field and the grain magnetization. An alternative explanation is that this behavior is due to unmodeled interactions between the tetrataenite grain and the kamacite matrix.

4 Discussion and Implications

4.1 Ideal Tetrataenite Grain Geometry

In the absence of a pseudo-single domain state like a single vortex state, tetrataenite is stable against viscous relaxation and external field remagnetization in both its SD and two-domain states. The size range of the SD stability field varies with axial ratio; for equant grains it ranges from 6 to 64 nm. Below 6 nm, tetrataenite is in a SP state. Above 64 nm, tetrataenite occupies a two-domain state. However, in the presence of an external field on the order of 100 mT, a two-domain grain can be placed into a uniform state through the destruction of its domain wall (Section 3.2, Fig. 5). Additionally, the magnetization of a two-domain grain or a SD grain in the two-domain stability field is stable over the lifetime of the solar system. Therefore, we propose that tetrataenite is stable even at sizes above the SD range in the absence of heating or strong external fields, though we are unable to conduct micromagnetic models to place an upper bound on the stability range once tetrataenite forms more than two domains.

Tetrataenite grains in cloudy zones, the adjacent rims, and in plessite range in diameter from tens of nm to ~10 µm (Goldstein et al., 2017; Goldstein et al., 2009; Goldstein et al., 2014; Nichols et al., 2020; Yang et al., 2007, 2010). We can compare the grain sizes reported in previous studies with the SP-SD-two domain threshold (Fig. 2) to determine their magnetic stability. Among the meteorite groups that were the subject of paleomagnetic studies, the fast-cooled IVA irons are the only group with cloudy zone tetrataenite grains all falling in the SD region (Nichols et al., 2020). Two other meteorite groups, the IVB and IIIAB irons, have islands that fall exclusively in the SD stability field but have not been studied with paleomagnetism. Otherwise, tetrataenite grain sizes in cloudy zones fall either partly inside or all outside the SD stability field. For example, the IAB iron meteorites possess island sizes that fall partly in the SD range for elongated grains while the mesosiderites show islands that only fall outside the SD stability field. Mesosiderite tetrataenite islands are reported to exhibit MD behavior (Nichols et al., 2020) and IAB islands close to the clear tetrataenite rim appear SD (J. F. J. Bryson et al., 2014b). However, the spatial resolution of XPEEM [30 nm; (Stöhr et al., 1998)] prevents the determination of individual island domain states.

While we are unable to conduct micromagnetic modeling of tetrataenite grains with least energy states containing more than two domains, a combination of

analytical calculations and observations from imaging of tetrataenite domains in the tetrataenite rim abutting cloudy zones and large tetrataenite grains in plessite can constrain the extent of the two-domain region (Fig. 2). The tetrataenite rim ranges in size from 200 nm to 10 µm depending on the cooling rate (Goldstein et al., 2017; Uehara et al., 2011). Faster cooled meteorites, such as the Steinbach and Chinautla IVA irons, are reported to have 200-nm rims and possess magnetic domains < 2 µm long (J. F. J. Bryson et al., 2017; Nichols et al., 2020). In comparison, the slow-cooled Estherville mesosiderite has a 5 µm-wide clear tetrataenite rim with magnetic domains that are ~200-300 nm wide and up to 3 µm long (Nichols et al., 2020). Analytical calculations predict that the transition from a two-domain to a three-domain state occurs at ~360 nm for cubic tetrataenite grains, which could be compatible with the 200-300 nm width of the observed domains in the tetrataenite rim, though the axial ratio of the tetrataenite rim is difficult to define as the rim runs along the full length of the cloudy zone.

Akin to the tetrataenite rim, large tetrataenite islands and individual tetrataenite grains outside of the cloudy zone microstructure can be multidomain (Nichols et al., 2020; Uehara et al., 2011). For example, the Estherville mesosiderite has islands as large as 463 ± 32 nm (Goldstein et al., 2014). Such sizes fall in the two- or three-domain stability field depending on the axial ratio (Fig. 2) and are reported to be multidomain (Nichols et al., 2020). Ordinary chondrites contain zoneless plessite grains with m-sized tetrataenite grains and are interpreted to be multidomain as well based on the low macrocoercivity of the grains compared to the cloudy zone (Uehara et al., 2011).

4.2 Role of Island-Island Interactions in Cloudy Zone Tetrataenite.

In our micromagnetic modeling, we focus on individual tetrataenite grains and ignore interactions between grains to elucidate the natural domain states of tetrataenite. However, the mutual proximity of tetrataenite islands (<1-2 island diameters) in the cloudy zone suggests that island-island magnetostatic interactions should be considered. Micromagnetic modeling of cloudy zone islands from the Tazewell IAB iron meteorite (Einsle et al., 2018) showed that the transition of taenite to tetrataenite through an increase in the magnetocrystalline anisotropy constant forced a taenite SV state into a tetrataenite grain with two oppositely pointing magnetization domains and a domain wall. The two-domain structure is similar to that seen in our simulations. Magnetostatic interactions between the islands act to displace the grain wall until it is destroyed, creating SD islands. This process is akin to the application of an external field in the hysteresis loops shown in Figure 5, which forces out the domain wall at H_W. Treating a cubic tetrataenite island of volume v like a simple dipole with a magnetization m equal to its saturation magnetization, the external field B created by that grain at a distance r follows

$B = \frac{\mu_0 v M_s}{2\pi r^3}$.

At the center of a neighboring island of the same size, that field produce by

the tetrataenite cube is ~275 mT, though the field could be larger or smaller depending on the geometry of the island and its neighbor. This field is the same order of magnitude as H_W for the grains we modeled, indicating that magnetostatic interactions could indeed provide a method of destroying the domain wall in a two-domain grain. However, the strength of the island-island interactions remains to be quantified.

Our results support the idea that magnetostatic interactions between islands is of fundamental importance in the ability of cloudy zones to preserve the record of ancient magnetic fields. As the external field necessary to completely destroy the domain wall is on the order of hundreds of mT, which is orders of magnitude stronger than any reported planetesimal dynamo [less than a few hundred T (Maurel et al., 2021)], the identification of uniform magnetization across cloudy zone islands is likely solely due to magnetostatic interactions. If no magnetostatic interactions were present, then grains above the SD – two domain threshold would be expected to be two-domain if XPEEM resolution was capable of imaging individual island magnetization. While the two-domain state is stable, additional work must be conducted to determine how to interpret the paleomagnetic record of this domain state. If an external field is present, it could bias the destruction of domain walls via island-island interaction in a certain direction, creating the preference of islands toward one easy axis as seen in XPEEM images (J. F. J. Bryson et al., 2014b).

We propose that that magnetostatic interactions have a direct influence on the ability of cloudy zones to be suitable for paleomagnetic analyses and allow for slower cooling rates that would otherwise lead to islands sizes above the SD – two domain threshold. This proposal is in contrast to the conclusions of Nichols et al. (2020) that magnetostatic interactions do not have an influence on determining which cloudy zones can be studied with paleomagnetism since our results show that magnetostatic interactions are fundamental in placing the islands in an SD state. However, like Nichols et al. (2020), we agree that magnetostatic interactions do not play a role in affecting whether the cloudy zone shows evidence of a past magnetic field since the destruction of the domain wall is due to island-island interactions based on the strength of the field necessary to destroy the domain wall.

4.3 Comparison of Predicted and Observed Tetrataenite Coercivities

As detailed in Section 3.2.2, the coercivities of individual tetrataenite grains based on our simulated hysteresis loops range from 1 – 2.6 T depending on the size and axial ratio (Fig. 6). The trend of decreasing coercivity with increasing grain size is consistent with observations of tetrataenite coercivities from J. F. J. Bryson et al. (2014a) and Uehara et al. (2011). However, the reported coercivities of tetrataenite islands in the cloudy zone (~1 T or less) that are within the size range encompassed by our models are lower than predicted from our hysteresis loops (Fig. 6), This suggests that either our model is not predicting the correct coercivities, or that interactions between islands or between islands and the surface of the antitaenite matrix in cloudy zones have an effect on the island

coercivities that cannot be observed in our micromagnetic modeling. The proposal that the matrix affects island coercivities is supported by micromagnetic simulations conducted on cloudy zone tetrataenite in a "soft" magnetic matrix which leads to a decrease in coercivity as a results of exchange coupling between the islands and the matrix (J. F. J. Bryson et al., 2014a). While antitaenite has unambiguously been identified as the matrix phase between tetrataenite island through Mössbauer spectroscopy (Blukis et al., 2017), the paramagnetic nature of the phase is inconsistent with the magnetically-soft ferromagnetic phase seen in XPEEM images [e.g. (Nichols et al., 2020)]One potential explanation for this discrepancy is that the stress at the surface of the cut face of samples could allow a magnetic structure to stabilize (Blukis et al., 2017). If this is case, it is uncertain whether the tetrataenite islands would have a larger effect on the stable magnetic structure of the matrix phase, or if the matrix phase impacts the islands to a greater extent.

The large grain sizes of the tetrataenite in the Bacubirito plessite do not allow for direct comparison between our modeled and observed coercivities. Assuming the curves can be propagated at larger sizes using a Lorentzian fit, we can provide a tentative estimate of the coercivity provided for larger grains by our model (Supplementary Fig. S1). At 400 nm, predicted coercivities range between ~850 mT and ~1,050 mT depending on the axial ratio. These are higher than the observed coercivities of the uniformly magnetized grains, the majority of which fall between 250 mT and 324 mT. The difference between the observed and predicted coercivities could indicate some interaction between the tetrataenite and the matrix kamacite as suggested for cloudy zone tetrataenite, but we caution that there is no guarantee that the size – coercivity relationship seen in our models is consistent out to such large grain sizes. Our modeled coercivities only span the SD stability field and the lower grain sizes of two-domain stability field. These trends might not be applicable to larger two-domain grains and higher-domain grains, especially as the coercivities appear to plateau at larger grain sizes in our model.

4.4 Using Individual Tetrataenite for Paleomagnetic Studies

Obtaining accurate records of the intensity and direction of past magnetic fields from isolated, non-interacting tetrataenite grains (e.g., in plessite) remains to be solved. One limitation is that while XPEEM experiments can image the magnetization direction of tetrataenite with high-spatial resolution, the large spacing between grains means that the number of grains necessary to have a statistically meaningful dataset [~10^4 for a 1 degree discrepancy in the recovered paleodirection compared to the true paleodirection; (Berndt et al., 2016)] could make XPEEM time consuming and labor intensive. For Bacubirito duplex plessite, we can capture about ~100 grains per XPEEM image (not all of which are SD), compared to the many hundreds of grains in cloudy zone XPEEM images and several thousands of grains imaged over the course of a cloudy zone study.

If the tetrataenite grains are dispersed amongst non-magnetic materials such as silicate grains (Fig.1c), the magnetization could be studied using a super-

conducting moment magnetometer or superconducting quantum interference device (SQUID) microscope depending on the strength of the magnetic moment (Lima & Weiss, 2016). However, additional work needs to be conducted to determine how to interpret tetrataenite paleomagnetism, which is complicated by the uniaxial anisotropy of tetrataenite and the importance of crystallographic orientation in magnetization direction. This is different from cloudy zone paleomagnetic studies that take advantage of the effect of external fields on island-island interactions to bias the similarly crystallographic-oriented cloudy zone in the directly of the external field (Nichols et al., 2020).

5 Conclusions

Tetrataenite is a potent magnetic recorder that to date has only been utilized in paleomagnetic studies through investigations of the cloudy zone microstructure. However, tetrataenite can occur as individual, non-interacting grains in a variety of meteorite groups including irons, ordinary chondrites, and primitive achondrites. Understanding the fundamental magnetic properties and domain behavior of tetrataenite is not only important in order to further our understanding of the cloudy zone, but also to take a step towards expanding our ability to conduct paleomagnetic investigations of meteorites using individual tetrataenite grains.

Here, we propose a description of the domain state of non-interacting tetrataenite as a function of grain geometry based on fundamental magnetic principles and micromagnetic modeling. Tetrataenite in the size range of ~10 to ~160 nm occupies a uniform, SD state dependent on the grain's axial ratio. More elongated grains adopt the SD state as least-energy state at larger sizes compared to more equant grains. These grains possess relaxation times greater than the lifetime of the solar system. Below 6 nm, tetrataenite occupies a SP state. Once tetrataenite is too large to occupy a uniform state, the least-energy domain configuration is a two-domain state with the domains and domain wall parallel to the direction of uniaxial anisotropy. This is observed in XMCD images of tetrataenite in the ungrouped Bacubirito iron meteorite. Importantly, tetrataenite cannot occupy a vortex state due to the high uniaxial anisotropy of the mineral. The high uniaxial anisotropy also allows the two-domain state to be stable over the lifetime of the solar system.

Through the application of an external field, the two-domain state can be forced into a uniform state through a destruction of the domain wall. The subsequent uniform state can be retained even after the external field is removed. The majority of paleomagnetic cloudy zone studies rely of tetrataenite islands, whose sizes fall in the two-domain state range. However, magnetostatic interactions between islands provide a method of displacing the domain wall and creating single domain tetrataenite. Therefore, island-island interactions play a vital role in making the cloudy zone a useful paleomagnetic recorder, without which it would be more be more challenging to interpret XPEEM data.

Acknowledgments

We acknowledge and thank funding from NASA FINESST Grant 80NSSC20K1366 and NASA contract NNM16AA09C, "Psyche: Journey to a Metal World." We also acknowledge funding from the UK Natural Environment Research Council Grants (NERC) grants NE/S011978/1 and NE/S001018/1 to W.W. C.M. acknowledges the financial support of the European Marie Slokowska Curie Actions. We are grateful for the help of Dr. Santiago Benavides who provided assistance in setting up our modeling on the MIT Engaging Cluster. Additionally, we thank Les Nagy for productive conversations and suggestions for implementing MERRILL for this study. We also thank the Harvard Museum of Natural History for providing a sample of Bacubirito for our study. Lastly, we thank Rajesh Chopdekar and the Advance Light Source (ALS) at Lawrence Berkeley National Lab for setting up and maintaining the photon beam responsible for gathering our XPEEM data. This research used resources of the Advanced Light Source, a U.S. DOE Office of Science User Facility under contract no. DE-AC02-05CH11231.

Open Research Statement

All data needed to assess the conclusions stated in the paper can be found in the paper or in the Supplementary Material. Version 1.6.4 of the MERRILL micromagnetic modeling software can be freely downloaded at https://blogs.ed.ac.uk/rockmag/. The raw XPEEM data used for this study can be found on the Magnetics Information Consortium (MagIC) database at https://earthref.org/MagIC/19602/55003427-78f8-4df8-b2e7-3821179317b2.

References

Aharoni, A. (1998). Demagnetizing factors for rectangular ferromagnetic prisms. *Journal of Applied Physics, 83*(6), 3432-3434. Albertsen, J. F. (1981). Tetragonal lattice of tetrataenite (ordered fe-ni, 50-50) from 4 meteorites. *Physica Scripta, 23*(3), 301-306. Berndt, T., Muxworthy, A. R., & Fabian, K. (2016). Does size matter? Statistical limits of paleomagnetic field reconstruction from small rock specimens: Does size matter? *Journal of Geophysical Research, 121*(1), 15-26. Blukis, R., Pfau, B., Günther, C. M., Hessing, P., Eisebitt, S., Einsle, J., & Harrison, R. J. (2020). Nanoscale imaging of high-field magnetic hysteresis in meteoritic metal using x-ray holography. *Geochemistry, Geophysics, Geosystems, 21*(8), e2020GC009044. Blukis, R., Ruffer, R., Chumakov, A. I., & Harrison, R. J. (2017). A high spatial resolution synchrotron mossbauer study of the tazewell iiicd and esquel pallasite meteorites. *Meteorit Planet Sci, 52*(5), 925-936. Borlina, C. S., Weiss, B. P., Bryson, J. F. J., Bai, X., Lima, E. A., Chatterjee, N., & Mansbach, E. N. (2021). Paleomagnetic evidence for a disk substructure in the early solar system. *Science Advances, 7*(42), eabj6928. Bryson, J. F. J., Church, N. S., Kasama, T., & Harrison, R. J. (2014a). Nanomagnetic intergrowths in fe–ni meteoritic metal: The potential for time-resolved records of planetesimal dynamo fields. *Earth and Planetary Science Letters, 388*, 237-248. Bryson, J. F. J., Herrero-Albillos, J., Kronast, F., Ghidini, M., Redfern,

S. A. T., van der Laan, G., & Harrison, R. J. (2014b). Nanopaleomagnetism of meteoritic fe–ni studied using x-ray photoemission electron microscopy. *Earth and Planetary Science Letters, 396*, 125-133. Bryson, J. F. J., Nichols, C. I. O., Herrero-Albillos, J., Kronast, F., Kasama, T., Alimadadi, H., et al. (2015). Long-lived magnetism from solidification-driven convection on the pallasite parent body. *Nature, 517*(7535), 472-475. Bryson, J. F. J., Weiss, B. P., Biersteker, J. B., King, A. J., & Russell, S. S. (2020). Constraints on the distances and timescales of solid migration in the early solar system from meteorite magnetism. *The Astrophysical Journal, 896*(2). Bryson, J. F. J., Weiss, B. P., Getzin, B., Abrahams, J. N. H., Nimmo, F., & Scholl, A. (2019). Paleomagnetic evidence for a partially differentiated ordinary chondrite parent asteroid. *Journal of Geophysical Research, 124*(7), 1880-1898. Bryson, J. F. J., Weiss, B. P., Harrison, R. J., Herrero-Albillos, J., & Kronast, F. (2017). Paleomagnetic evidence for dynamo activity driven by inward crystallisation of a metallic asteroid. *Earth and Planetary Science Letters, 472*, 152-163. Buchwald, V. F. (1975). *Handbook of iron meteorites*: University of California Press.87-112.Butler, R. F., & Banerjee, S. K. (1975a). Single-domain grain size limits for metallic iron. *Journal of Geophysical Research, 80*(2), 252-259. Butler, R. F., & Banerjee, S. K. (1975b). Theoretical single-domain grain size range in magnetite and titanomagnetite. *Journal of Geophysical Research (1896-1977), 80*(29), 4049-4058. Butler, R. F., & Banerjee, S. K. (1975c). Theoretical single-domain grain size range in magnetite and titanomagnetite. *Journal of Geophysical Research, 80*(29), 4049-4058. Clark, D. A. (1984). Hysteresis properties of sized dispersed monoclinic pyrrhotite grains. *Geophysical Research Letters, 11*(3), 173-176. Conbhuí, P. Ó., Williams, W., Fabian, K., Ridley, P., Nagy, L., & Muxworthy, A. R. (2018). Merrill: Micromagnetic earth related robust interpreted language laboratory. *Geochemistry, Geophysics, Geosystems, 19*(4), 1080-1106. Cournede, C., Gattacceca, J., Gounelle, M., Rochette, P., Weiss, B. P., & Zanda, B. (2015). An early solar system magnetic field recorded in cm chondrites. *Earth and Planetary Science Letters, 410*, 62-74. Dos Santos, E., Gattacceca, J., Rochette, P., Fillion, G., & Scorzelli, R. B. (2015). Kinetics of tetrataenite disordering. *Journal of Magnetism and Magnetic Materials, 375*, 234-241. Dunlop, D. (2021). Magnetic hysteresis of magnetite, pyrrhotite and hematite at high temperature. *Geophysical Journal International, 225*(1), 1-14. Dunlop, D., & Özdemir, Ö. (1997). *Rock magnetism: Fundamentals and frontiers* (1 ed.): Cambridge University Press.83-144.Einsle, J. F., Eggeman, A. S., Martineau, B. H., Saghi, Z., Collins, S. M., Blukis, R., et al. (2018). Nanomagnetic properties of the meteorite cloudy zone. *Proceedings of the National Academy of Sciences, 115*(49), E11436-E11445. Einsle, J. F., Harrison, R. J., Kasama, T., Conbhuí, P. Ó., Fabian, K., Williams, W., et al. (2016). Multi-scale three-dimensional characterization of iron particles in dusty olivine: Implications for paleomagnetism of chondritic meteorites. *American Mineralogist, 101*(9), 2070-2084. Evans, M. E., & Mcelhinny, M. W. (1969). An investigation of the origin of stable remanence in magnetite-bearing igneous rocks. *Journal of Geomagnetism and Geoelectricity, 21*(4), 757-773. Fabian, K., & Shcherbakov, V. P. (2018). Energy barriers in three-dimensional micromagnetic models and the physics of thermoviscous

magnetization. *Geophysical Journal International, 215*(1), 314-324. Fu, R. R., Lima, E. A., & Weiss, B. P. (2014a). No nebular magnetization in the allende cv carbonaceous chondrite. *Earth and Planetary Science Letters, 404*, 54-66. Fu, R. R., Weiss, B. P., Lima, E. A., Harrison, R. J., Bai, X.-N., Desch, S. J., et al. (2014b). Solar nebula magnetic fields recorded in the semarkona meteorite. *Science, 346*(6213), 1089-1092. Fu, R. R., Weiss, B. P., Shuster, D. L., Gattacceca, J., Grove, T. L., Suavet, C., et al. (2012). An ancient cored dynamo in asteroid vesta. *Science, 338*(6104), 238-241. Garrick-Bethell, I., & Weiss, B. P. (2010). Kamacite blocking temperatures and applications to lunar magnetism. *Earth and Planetary Science Letters, 294*(1), 1-7. Gattacceca, J., Rochette, P., Scorzelli, R. B., Munayco, P., Agee, C., Quesnel, Y., et al. (2014). Martian meteorites and martian magnetic anomalies: A new perspective from nwa 7034: Martian meteorites & magnetic anomalies. *Geophysical Research Letters, 41*(14), 4859-4864. Gattacceca, J., Weiss, B. P., & Gounelle, M. (2016). New constraints on the magnetic history of the cv parent body and the solar nebula from the kaba meteorite. *Earth and Planetary Science Letters, 455*, 166-175. Goldstein, J. I., Huss, G. R., & Scott, E. R. D. (2017). Ion microprobe analyses of carbon in fe–ni metal in iron meteorites and mesosiderites. *Geochimica et Cosmochimica Acta, 200*, 367-407. Goldstein, J. I., & Michael, J. R. (2006). The formation of plessite in meteoritic metal. *Meteoritics & Planetary Science, 41*(4), 553-570. Goldstein, J. I., Scott, E. R. D., & Chabot, N. L. (2009). Iron meteorites: Crystallization, thermal history, parent bodies, and origin. *Geochemistry, 69*(4), 293-325. Goldstein, J. I., Yang, J., & Scott, E. R. D. (2014). Determining cooling rates of iron and stony-iron meteorites from measurements of ni and co at kamacite–taenite interfaces. *Geochimica et Cosmochimica Acta, 140*, 297-320. Lima, E. A., & Weiss, B. P. (2016). Ultra-high sensitivity moment magnetometry of geological samples using magnetic microscopy: Ultra-sensitive moment magnetometry. *Geochemistry, Geophysics, Geosystems, 17*(9), 3754-3774. Mansbach, E. N., Weiss, B. P., Borlina, C. S., & Lima, E. A. (2022). *Paleomagnetism of the acapulco primitive achondrite.* Paper presented at the Lunar and Planetary Science Conference. Maurel, C., Bryson, J. F. J., Lyons, R. J., Ball, M. R., Chopdekar, R. V., Scholl, A., et al. (2020). Meteorite evidence for partial differentiation and protracted accretion of planetesimals. *Science Advances, 6*(30), eaba1303. Maurel, C., Bryson, J. F. J., Shah, J., Chopdekar, R. V., T. Elkins-Tanton, L., A. Raymond, C., & Weiss, B. P. (2021). A long-lived planetesimal dynamo powered by core crystallization. *Geophysical Research Letters, 48*(6). Maurel, C., Weiss, B. P., & Bryson, J. F. J. (2019). Meteorite cloudy zone formation as a quantitative indicator of paleomagnetic field intensities and cooling rates on planetesimals. *Earth and Planetary Science Letters, 513*, 166-175. Muxworthy, A. R., Dunlop, D. J., & Williams, W. (2003). High-temperature magnetic stability of small magnetite particles. *Journal of Geophysical Research, 108*(B5). Muxworthy, A. R., & Williams, W. (2006). Critical single-domain/multidomain grain sizes in noninteracting and interacting elongated magnetite particles: Implications for magnetosomes. *Journal of Geophysical Research, 111*(B12), n/a-n/a. Muxworthy, A. R., & Williams, W. (2015). Critical single-domain grain sizes in elongated

iron particles: Implications for meteoritic and lunar magnetism. *Geophysical Journal International, 202*(1), 578-583. Nagy, L., Williams, W., Muxworthy, A. R., Fabian, K., Almeida, T. P., Conbhuí, P. Ó., & Shcherbakov, V. P. (2017). Stability of equidimensional pseudo–single-domain magnetite over billion-year timescales. *Proceedings of the National Academy of Sciences, 114*(39), 10356-10360. Nagy, L., Williams, W., Tauxe, L., Muxworthy, A. R., & Ferreira, I. (2019). Thermomagnetic recording fidelity of nanometer-sized iron and implications for planetary magnetism. *Proceedings of the National Academy of Sciences, 116*(6), 1984. Néel, L. (1955). Some theoretical aspects of rock-magnetism. *Advances in Physics, 4*(14), 191-243. Néel, L., Pauleve, J., Pauthenet, R., Laugier, J., & Dautreppe, D. (1964). Magnetic properties of an iron—nickel single crystal ordered by neutron bombardment. *Journal of Applied Physics, 35*(3), 873-876. Nichols, C. I. O., Bryson, J. F. J., Blukis, R., Herrero-Albillos, J., Kronast, F., Rüffer, R., et al. (2020). Variations in the magnetic properties of meteoritic cloudy zone. *Geochemistry, Geophysics, Geosystems, 21*(2), e2019GC008798. Nichols, C. I. O., Bryson, J. F. J., Herrero-Albillos, J., Kronast, F., Nimmo, F., & Harrison, R. J. (2016). Pallasite paleomagnetism: Quiescence of a core dynamo. *Earth and Planetary Science Letters, 441*, 103-112. Nichols, C. I. O., Krakow, R., Herrero-Albillos, J., Kronast, F., Northwood-Smith, G., & Harrison, R. J. (2018). Microstructural and paleomagnetic insight into the cooling history of the iab parent body. *Geochimica et Cosmochimica Acta, 229*, 1-19. Reisener, R. J., & Goldstein, J. I. (2003). Ordinary chondrite metallography: Part 2. Formation of zoned and unzoned metal particles in relatively unshocked h, l, and ll chondrites. *Meteoritics & Planetary Science, 38*(11), 1679-1696. Ricci, J. C. D., & Kirschvink, J. L. (1992). Magnetic domain state and coercivity predictions for biogenic greigite (fe3s4): A comparison of theory with magnetosome observations. *Journal of Geophysical Research, 97*(B12). Shah, J., Williams, W., Almeida, T. P., Nagy, L., Muxworthy, A. R., Kovács, A., et al. (2018). The oldest magnetic record in our solar system identified using nanometric imaging and numerical modeling. *Nature Communications, 9*(1). Soffel, H. (1976). Pseudo-single-domain effects and single-domain multidomain transition in natural pyrrhotite deduced from domain structure observations. *Journal of Geophysics, 42*(1), 351-359. Stöhr, J., Padmore, H. A., Anders, S., Stammler, T., & Scheinfein, M. R. (1998). Principles of x-ray magnetic dichroism spectromicroscopy. *Surface Review and Letters, 05*(06), 1297-1308. Tauxe, L. (2010). *Essentials of paleomagnetism*: University of California Press.512.Uehara, M., Gattacceca, J., Leroux, H., Jacob, D., & van der Beek, C. J. (2011). Magnetic microstructures of metal grains in equilibrated ordinary chondrites and implications for paleomagnetism of meteorites. *Earth and Planetary Science Letters, 306*(3), 241-252. Weiss, B. P., Bai, X., & Fu, R. R. (2021). History of the solar nebula from meteorite paleomagnetism. *Science Advances, 7*(1), eaba5967. Weiss, B. P., Berdahl, J. S., Elkins-Tanton, L., Stanley, S., Lima, E. A., & Carporzen, L. (2008a). Magnetism on the angrite parent body and the early differentiation of planetesimals. *Science, 322*(5902), 713-716. Weiss, B. P., Fong, L. E., Vali, H., Lima, E. A., & Baudenbacher, F. J. (2008b). Paleointensity of the ancient martian magnetic field. *Geophysical Research Letters, 35*(23),

L23207. Weiss, B. P., Gattacceca, J., Stanley, S., Rochette, P., & Christensen, U. R. (2010). Paleomagnetic records of meteorites and early planetesimal differentiation. *Space Science Reviews, 152*(1-4), 341-390. Willis, J., & Goldstein, J. I. (1983). A three-dimensional study of metal grains in equilibrated, ordinary chondrites. *Journal of Geophysical Research, 88*(S01). Yang, J., Goldstein, J. I., & Scott, E. R. D. (2007). Iron meteorite evidence for early formation and catastrophic disruption of protoplanets. *Nature, 446*(7138), 888-891. Yang, J., Goldstein, J. I., & Scott, E. R. D. (2010). Main-group pallasites: Thermal history, relationship to iiiab irons, and origin. *Geochimica et Cosmochimica Acta, 74*(15), 4471-4492.

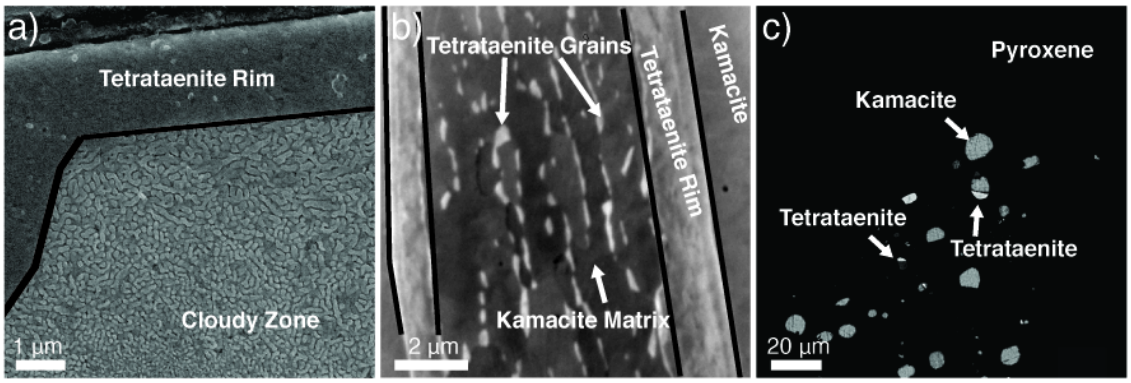

Figure 1: Occurrences of tetrataenite in various meteorite groups. **a)** Secondary electron image of the cloudy zone and adjacent clear tetrataenite rim in the Ankober H chondrite. Tetrataenite islands decrease in size as distance from the clear tetrataenite rim increase due to lower Ni concentrations. Image taken on a Merlin Zeiss FEG-SEM at the MIT Material Research Laboratory. **c)** X-ray photoelectron emission microscopy (XPEEM) image of duplex plessite, an intergrowth of taenite/tetrataenite and kamacite formed from decomposition of martensite with precipitates >200 nm (Goldstein & Michael, 2006; Zhang et al., 1993), in the Bacubirito ungrouped iron meteorite taken at the Advanced Light Source of the Lawrence Berkeley National Laboratory. Gray scale is indicative of nickel content. The individual tetrataenite grains stand out from the kamacite matrix due to their higher concentrations of Ni. **c)** Backscattered electron microscopy image of a pyroxene grain with metal blebs in the Acapulco primitive achondrite. The tetrataenite appears brighter compared to the kamacite due to its higher Ni content. Image taken on a JEOL JXA-8200 Superprobe electron microprobe machine at the Earth, Atmospheric, and Planetary Science Department at MIT.

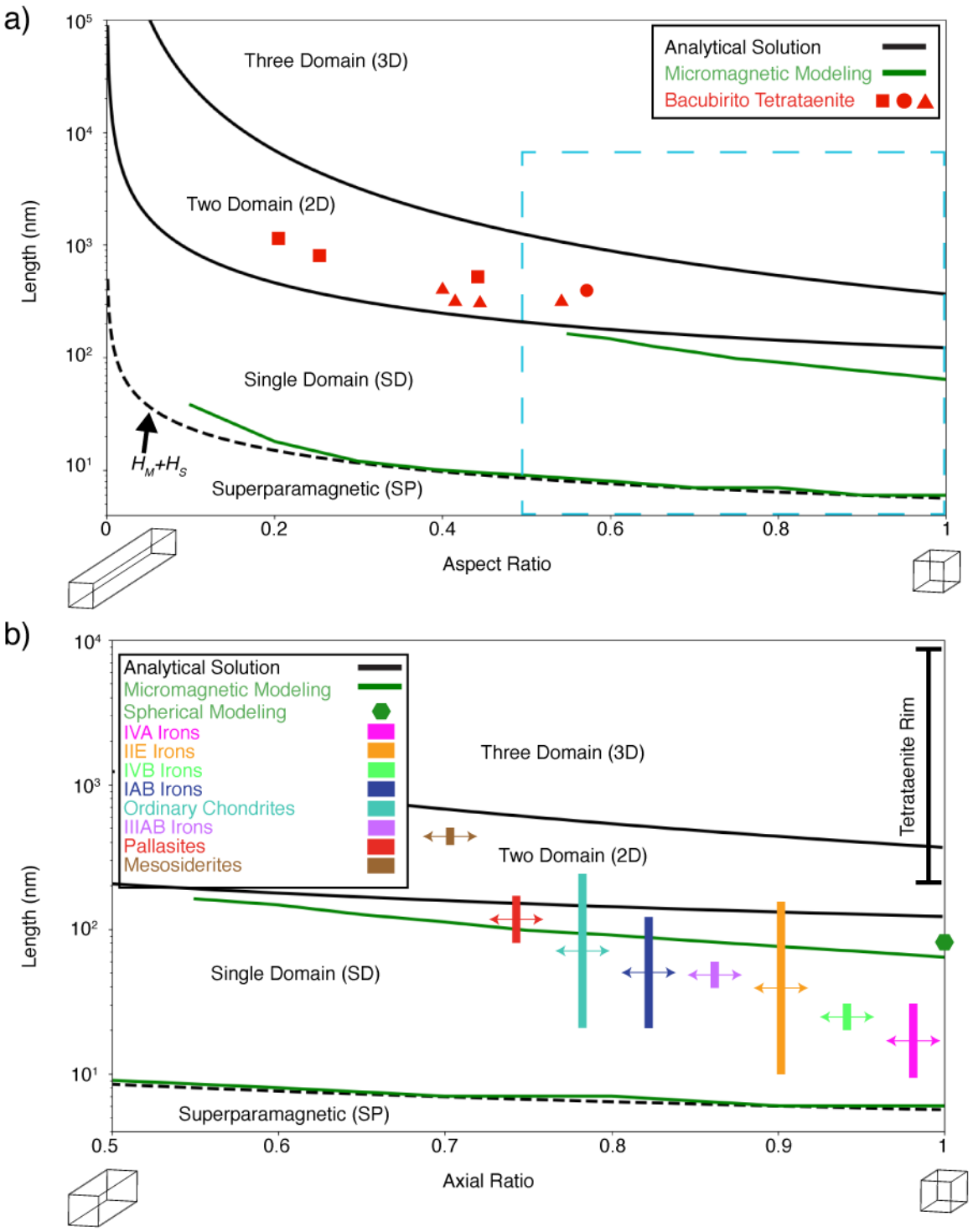
a)
Analytical Solution
Micromagnetic Modeling
Bacubirito Tetrataenite
Three Domain (3D)
Two Domain (2D)
Single Domain (SD)
H_M+H_S
Superparamagnetic (SP)
Length (nm)
Aspect Ratio
b)
Analytical Solution
Micromagnetic Modeling
Spherical Modeling
IVA Irons
IIE Irons
IVB Irons
IAB Irons
Ordinary Chondrites
IIIAB Irons
Pallasites
Mesosiderites
Three Domain (3D)
Two Domain (2D)
Single Domain (SD)
Superparamagnetic (SP)
Tetrataenite Rim
Length (nm)
Axial Ratio

Figure 2: Domain states of tetrataenite as a function of length and axial ratio. **a)** Full results of the domain states of tetrataenite. Analytical solution and results of micromagnetic modeling are shown. The analytical solutions follow Equations (2), (3), and (5), and the SP-SD threshold is presented for the uniaxial and shape anisotropy easy axes oriented in the same direction. Red shapes denote tetrataenite grains observed in the Bacubirito meteorite, with triangles representing SD grains, circles representing two-domain grains, and squares representing grains with greater than two domains (Section 3.3). **b)** Close up of blue-dashed box in a). Vertical range of colored rectangles represent reported cloudy zone tetrataenite island sizes for selected meteorite groups (Blukis et al., 2020; J. F. J. Bryson et al., 2015; J. F. J. Bryson et al., 2019; J. F. J. Bryson et al., 2017; Einsle et al., 2018; Goldstein et al., 2017; Goldstein et al., 2009; Goldstein et al., 2014; Maurel et al., 2020; Maurel et al., 2021; Nichols et al., 2020; Yang et al., 2010). Since images of cloudy zone islands show a range of axial ratios, we allow each meteorite group to occupy the full width of the axial ratio domain, denoted by the doubled-sided arrow. The widths of reported tetrataenite rims are represented by the black bar. Green hexagon shows the SD-to-two-domain transition for spherical tetrataenite based on our micromagnetic calculations.

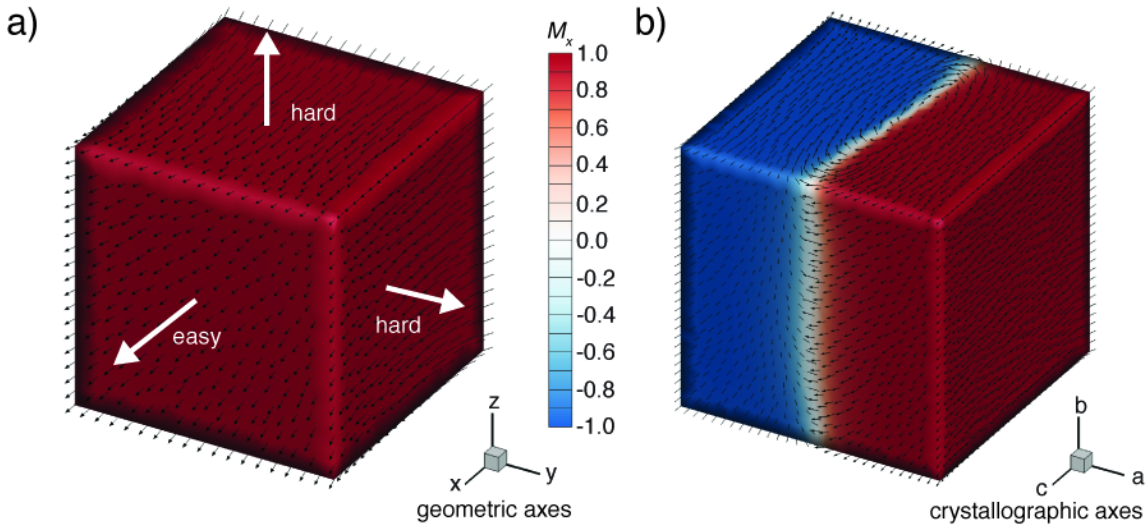

Figure 3: Domain states of tetrataenite from micromagnetic modeling. The magnetic easy axis is chosen to lie along the x-axis which is the crystallographic c-axis. Small black arrows represent the dipole direction associated with each element in the mesh and large white arrows show the orientations of the magnetic easy and hard axes, which are the same for both cubes. The color scale shows the relative intensity of the x-component of each dipole at the surface of the cube. **a)** 50 nm single-domain tetrataenite cube exhibiting "flower" behavior at the grain edges [e.g., (Muxworthy & Williams, 2006)]. **b)** 80-nm, two-domain

tetrataenite cube separated by a domain wall along the magnetic easy axis. The two domains are forced to point in the direction of the easy axis due to the high uniaxial anisotropy of tetrataenite.

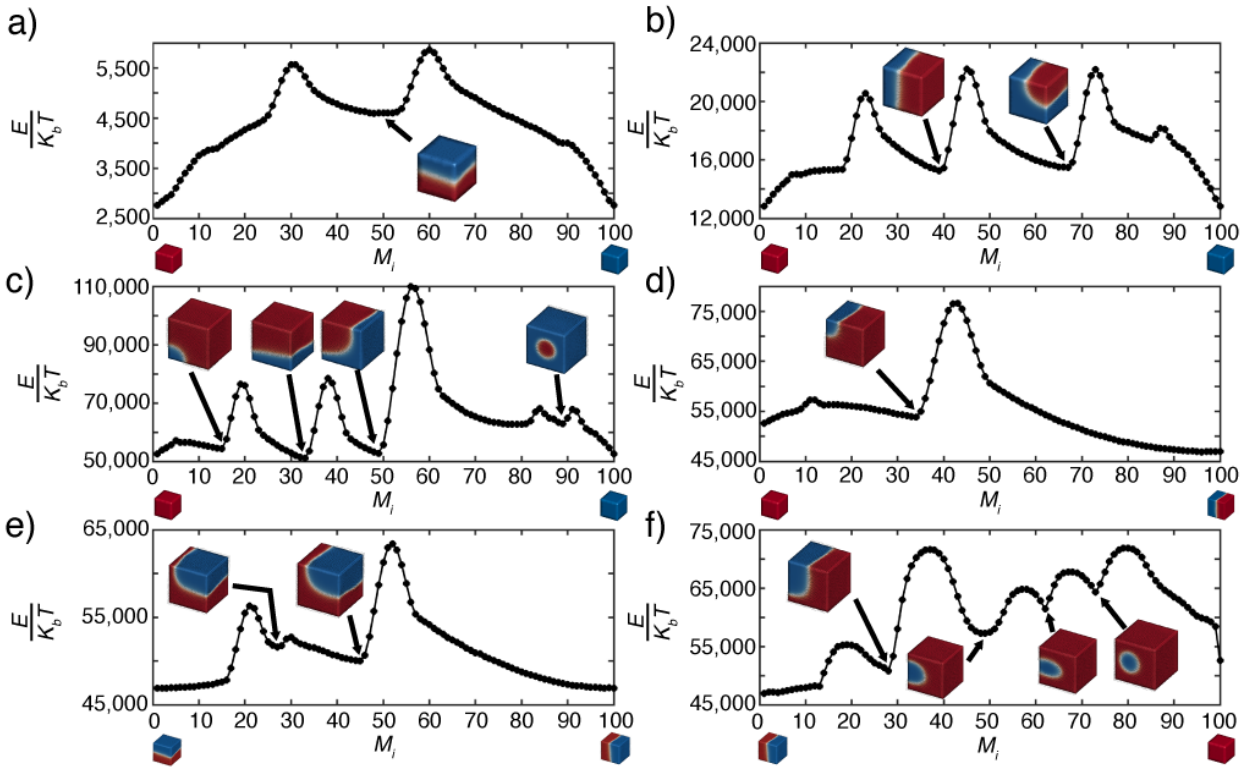

Figure 4: NEB paths (energy as a function of magnetization step) depicting the energy barriers between different domain states in tetrataenite grains of various sizes. The ordinate gives the total grain magnetic energy normalized to k_BT and the abscissa gives the magnetization steps M_i along the least energy path. **a)** 30 nm cube. Both the initial and final state are SD. **b)** 50-nm cube. Both initial and final state are SD. **c)** 80-nm cube. Both initial and final state are SD. **d)** 80-nm cube. Initial state is SD and final state is two-domain. **e)** 80-nm cube. Both initial and final state are two-domain but the final state domains are oriented perpendicular to the initial state domains. **f)** 80-nm cube. Initial state is two-domain and final state is SD. Three-dimensional renderings of metastable magnetization states along the NEB paths are shown by the cubes in each panel. Renderings of the initial states for each NEB path are shown below the start and end of each NEB path. The orientation of the renderings and color scale bar for magnetization along the x-axis are the same as in Figure 3.

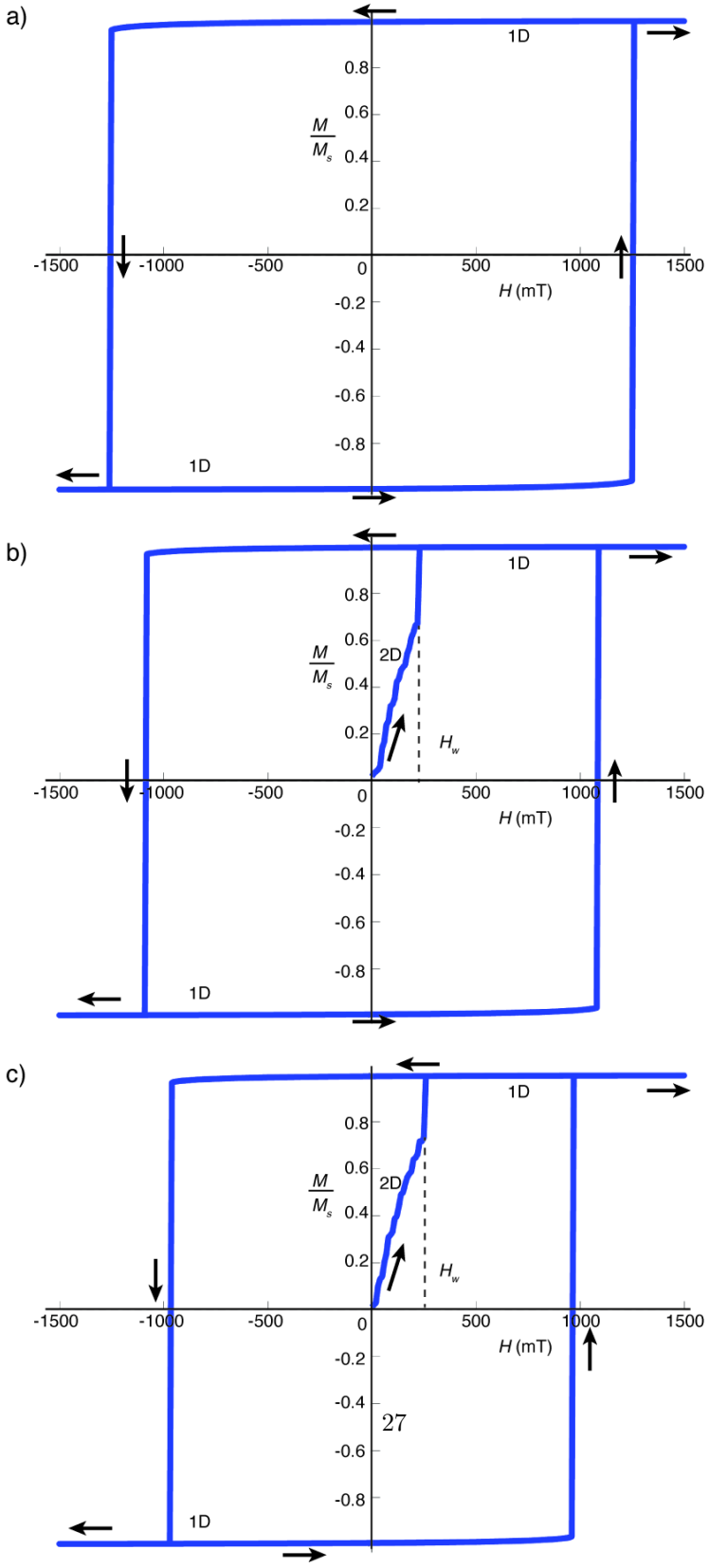
a)
1D
0.8
0.6
M/M_s
0.4
0.2
-1500
-1000
-500
0
500
1000
1500
H (mT)
-0.2
-0.4
-0.6
-0.8
1D
b)
1D
0.8
0.6
M/M_s
2D
0.4
0.2
H_w
-1500
-1000
-500
0
500
1000
1500
H (mT)
-0.2
-0.4
-0.6
-0.8
1D
c)
1D
0.8
0.6
M/M_s
2D
0.4
0.2
H_w
-1500
-1000
-500
0
500
1000
1500
H (mT)
-0.2
-0.4
-0.6
-0.8
1D

Figure 5: Simulated hysteresis loops of tetrataenite cube with sizes of **a)** 50 nm (SD), **b)** 70 nm (two-domain), and **c)** 100 nm (two-domain). The SD tetrataenite grain shown in a) exhibits classical SD hysteresis loops, remaining in a uniform state until its microcoercivity is reached and the magnetization flips to the opposite direction. Two-domain tetrataenite grains [e.g., 70 nm cube (b) and 100 nm cube (c)] have their domain walls destroyed at a critical field H_W and remain in a uniform state even after the field is removed.

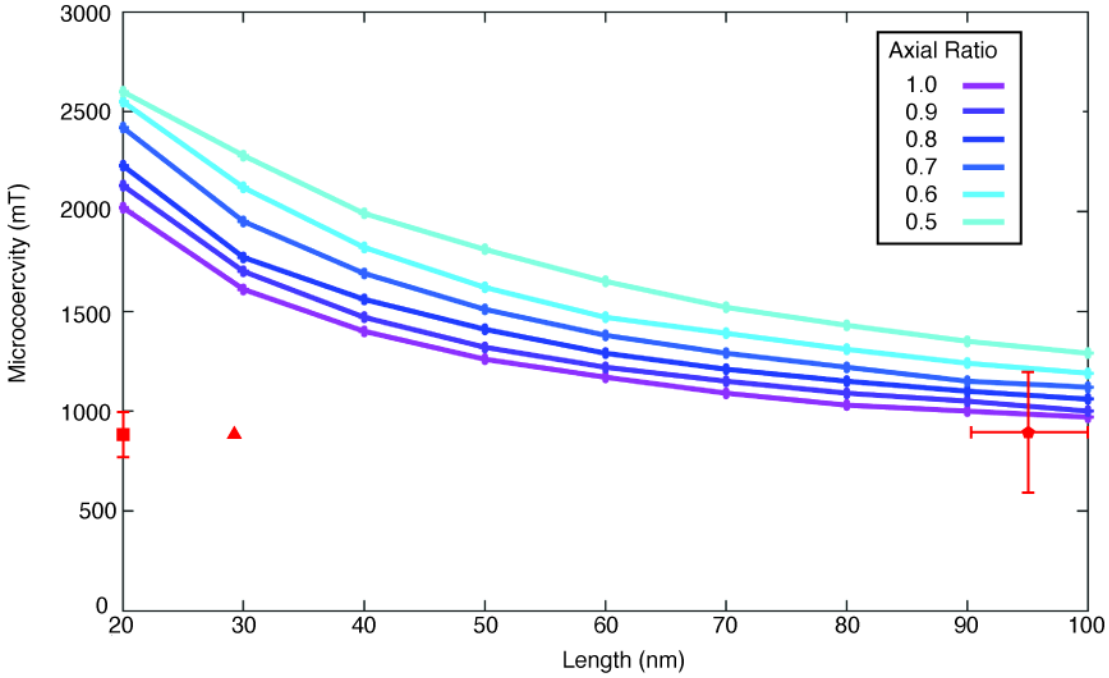

Figure 6: Microcoercivity of individual tetrataenite grains as a function of grain length and axial ratio. The coercivity increases with decreasing grain size and axial ratio. Empirical observations of cloudy zone tetrataenite coercivities in ordinary chondrites [square; (Uehara et al., 2011)], the Steinbach IVA iron [triangle, (J. F. J. Bryson et al., 2017)], and Tazewell IAB iron [pentagon; (J. F. J. Bryson et al., 2014a)] are shown in red.

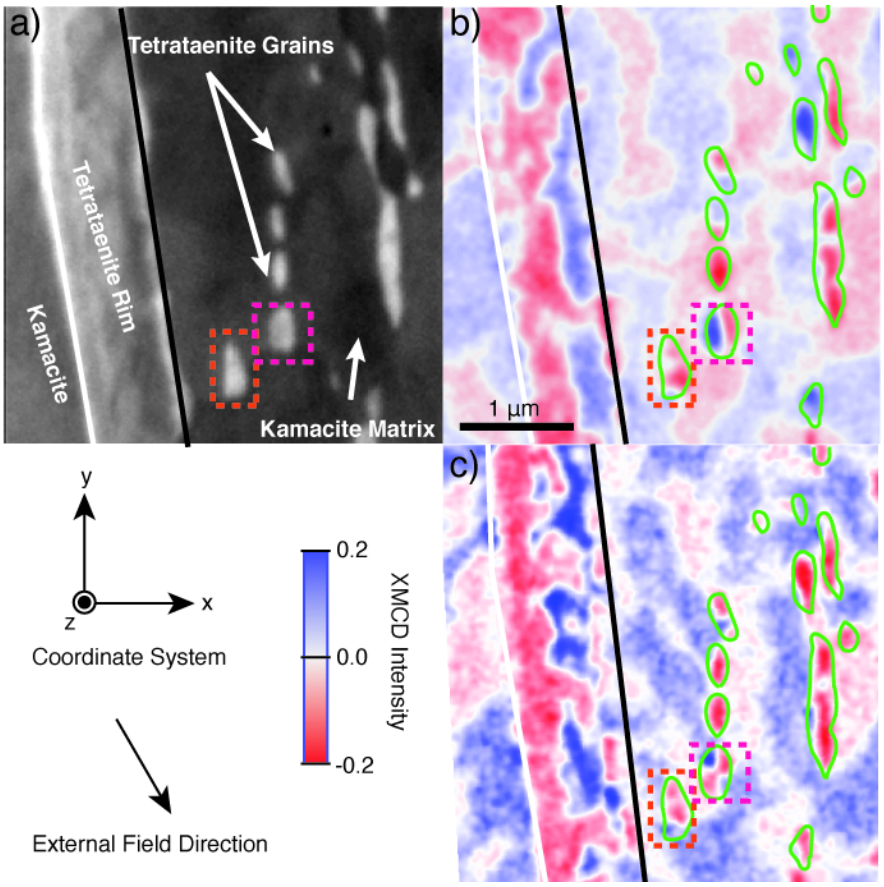

Figure 7: XPEEM and XMCD images of duplex plessite in Bacubirito. **a)** XPEEM image showing different components in duplex plessite: light colors correspond to high Ni content. **b)** Natural remanent magnetization XMCD image of the same field of view in a). **c)** XMCD image of the same field of view in a) after the application of a 324 mT external field. The coordinate system is shown in the bottom left as well as the direction of the external field. The pixel color represents the degree of magnetization alignment with the X-ray beam direction, which was in the x-direction and inclined 30° into the page. Blue (red) is aligned (anti-aligned) with the beam. The green outlines in b) and c) represent the shapes of the tetrataenite grains in a). The magenta and orange dashed boxes in a), b), and c) show the two-domain and the greater than two-domain tetrataenite grains, respectfully, discussed in the main text.